JOURNAL OF SOLID STATE CHEMISTRY 79, 263–276 (1989)

Crystal Structure and Magnetism in $MnSb_2O_6$: Incommensurate Long-Range Order

J. N. REIMERS AND J. E. GREEDAN

Institute for Materials Research and The McMaster Nuclear Reactor, McMaster University, Hamilton, Canada L8S 4M1

AND M. A. SUBRAMANIAN

E. I. du Pont de Nemours and Co., Experimental Station, Wilmington, Delaware 19898

Received October 3, 1988; in revised form December 1, 1988

$MnSb_2O_6$ was investigated by neutron diffraction and magnetic susceptibility techniques. The structure was trigonal, space group $P321$, $a = 8.8011(3)$ Å, $c = 4.7241(1)$ Å. Low-temperature neutron data gave no evidence of structural change down to 14 K. Inverse susceptibility data show a deviation from Curie–Weiss behavior below 200 K and the magnetization shows a maximum at 12 K associated with the onset of three-dimensional order. A Curie–Weiss law fit of the susceptibility data above 200 K gave an Mn^{2+} moment of 5.76(1) μ_B. The ordered magnetic structure as determined by neutron diffraction was incommensurate with the nuclear lattice and could be described by a propagation vector $\tau = (0.013, 0.013, 0.179)$ in reciprocal lattice units. Measured magnetic moments below T_c gave an extrapolated zero point moment of 4.6 μ_B for Mn^{2+} and critical parameters $\beta = 0.31(2)$ and $T_c = 11.92(5)$ K.

Introduction

The magnetic susceptibility and specific heat of tantalates of composition MTa_2O_6 with M = Fe, Co, or Ni show evidence for important two-dimensional correlations (*1*, *2*). To extend these studies to include compounds with other divalent and pentavalent ions the material $MnSb_2O_6$ was studied. A previous report suggested that this material crystallizes in the columbite structure (*3*). More recently a stronger similarity was noted between the X-ray powder patterns of $MnSb_2O_6$ and known trirutile phases $FeSb_2O_6$, $CoSb_2O_6$, and $NiSb_2O_6$, suggesting a trirutile polymorph (*4*). However, Scott (*5*) has shown that $MnSb_2O_6$, when prepared in air between 900 and 1100°C from MnO and Sb_2O_3, forms yet another structure which is trigonal. A detailed crystal structure for this phase was reported based on refinement of X-ray Guinier powder data. We carried out a further study of $MnSb_2O_6$ using powder neutron diffraction to confirm the structure reported in (*5*). One implication of the trigonal structure is that the Mn^{2+} ions are arranged in layers consisting of distorted hexagonal nets. As this feature might give rise to some unusual magnetic properties a detailed magnetic study including low-temperature neutron diffraction was also undertaken.

0022-4596/89 $3.00

Experimental Details

The $MnSb_2O_6$ sample was a yellow powder prepared according to the procedures of Ref. (*5*). Time-of-flight neutron diffraction data were collected at the Intense Pulsed Neutron Source (IPNS) at Argonne National Laboratory using the General Purpose powder diffractometer (GPPD). The sample was sealed in a thin-walled vanadium tube and data were collected at room temperature for about 12 hr. A general description of the time-of-flight method including principles of operation, resolution, line shape, background fitting, and specific information on the GPPD at IPNS including detector configuration and other details have been published (*6*). Data from the $2\theta = 150°$ detector bank were used exclusively in this work to afford the highest possible resolution. Data preparation and least-squares profile refinements were carried out using the programs RUNPLOT, TOFPRP, TOFLS, and TOFSTAN, respectively, of the IPNS Rietveld Analysis package (*7*). These programs are modifications of the original versions described by Von Dreele *et al.* (*8*).

The background was fit to a five-parameter function written as

$$Y_{bk} = b_0 + Iv\{b_1 + b_2D + b_3(-1 + 2D^2) + b_4(-3D + 4D^3) + b_5(1 - 8D^2 + 8D^4)\},$$

where $D = \{(2 \times \text{TOF/DIFC}) - 1\}$. DIFC is an instrument parameter determined by calibration, TOF is the time-of-flight of the data point considered, Iv is incident neutron intensity for a given TOF, and D increases with d-spacing. The peak shape function is the "Jorgensen" function described in (*6*). The peak width parameter $\sigma = [\sigma_0 + \sigma_1 d^2 + \sigma_2 d^4]^{1/2}$ includes contributions from the neutron pulse width σ_0, the instrument geometry σ_1, and particle size effects σ_2, where d is the d-spacing of the reflection being considered.

In the full-matrix least-squares refinement of the crystal structure the function $m = \Sigma\{w(Y_{obs} - Y_{calc})^2\}$ is minimized. Y_{obs} and Y_{calc} are the observed and calculated profile intensities at a particular time-of-flight value, respectively, and w is the weight which is proportional to the reciprocal of the observed intensity. The starting values of the positional parameters and cell constants were those determined by Scott (*5*) from X-ray powder diffraction, using a Guinier camera. Neutron scattering lengths were taken from Koester (*9*). No corrections for absorption, extinction, or preferred orientation were applied.

Low-temperature (7–14 and 30 K) and room-temperature data sets were collected at the McMaster Nuclear Reactor (MNR) using 1.3916 Å neutrons obtained from a [200] copper monochromator. Data were collected using a position sensitive detector (PSD) which is essentially the same as that in use at Missouri University Research Reactor (MURR) which has been described previously (*10*). Soller-type collimators are not currently used but an oscillating–rotating collimator (ORC) is in place between the sample and the PSD to reduce background levels. The resolution of the above system is similar to that of the facility at MURR but FWHM values for standard materials are 20–25% greater in the same 2θ range for samples of similar diameter. At the present sample-to-detector distance of 106 cm and the operating wavelength, useful data are collected over a 25° 2θ range for a single detector setting. Thus, a typical data set requires collection of four or five such frames.

The raw data are then corrected for detector geometry and refined according to the procedures of Ref. (*10*). Refinement is carried out with a version of the Rietveld profile refinement program as modified by A. W. Hewat and E. Prince with further modifications added locally by M. Eitel (*11*).

For the low-temperature data sets the

sample was loaded into a thin-walled aluminum can with helium carrier gas and the can was sealed with indium wire. Bragg peaks from the aluminum sample holder were subtracted from the data. This resulted in rather poor counting statistics in some small regions of the data set where large aluminum peaks occurred.

Magnetic data were collected on a PAR vibrating sample magnetometer using a pressed polycrystalline pellet between 4.2 and 300 K. Temperature was measured using a calibrated chromel–gold 0.07% iron thermocouple. The magnetometer was calibrated with a sample of high-purity nickel.

Results and Discussion

Structure Data 14 and 298 K

As expected the positions of the metal atoms are in good agreement with those obtained by Scott and larger discrepancies are present in the oxygen positional parameters. This is due to the weak X-ray scattering power of oxygen relative to the heavier metal atoms. These results are shown in Table I and the profile fits are shown in Figs. 1 and 2.

Comparing the room-temperature parameters with those observed at 14 K (also Table I) demonstrates that no significant structural change occurs at temperatures near the magnetic transition temperature.

As pointed out by Scott (*5*) the atomic positions of $MnSb_2O_6$ indicate a similarity with the Na_2SiF_6 structure (*12*) with a slightly different distribution of cations over the available sites.

Results from the refinement of the room-temperature data set from MNR are not reported as they were not significantly different from IPNS results.

However, the room-temperature cell volume from the MNR data set was 316.96(9) $Å^3$. When both MNR values (to avoid systematic errors between instruments) are compared one can see that within three standard deviations the cell volume remains unchanged down to 14 K. Anisotropic temperature factors were refined with the IPNS data but this resulted in nonpositive definite thermal motion tensors for both Mn and Sb at the 3f site, so isotropic thermal parameters are reported. For the same reason only an overall thermal parameter is reported for the 14 K structure.

Nearest-neighbor bond distances from the 298 K data are listed in Table II, and show no anomalous behavior when compared to values expected from summation of atomic radii (*13*).

The structure can be described as a close-packed network of edge-sharing oxygen octahedra, one-third containing Sb^{5+} and one-sixth containing Mn^{2+} as seen in Fig. 3. The $z = 0$ layer consists of finite edge-sharing clusters of three MnO_6 octahedra surrounding one SbO_6 unit. The $z = \frac{1}{2}$ layer is easily pictured as an infinite distorted honeycomb lattice of SbO_6 octahedra. The two layers are connected along the z-direction by corner sharing between MnO_6 and SbO_6 octahedra. Of particular interest is the magnetic sublattice of manganese atoms which consists of distorted triangular sheets (Fig. 4) stacked along the c-direction. These sheets can be described in terms of corner-sharing large and small equilateral triangles, the large triangles containing antimony in the center. The Mn atoms form straight chains along the c-direction.

Magnetic Susceptibility

Magnetization and inverse susceptibility data at an applied field of 3 kOe are shown in Figs. 5 and 6. The magnetization data show a maximum at $T_c \approx 12.5$ K indicating antiferromagnetic ordering. The inverse susceptibility deviates strongly from Curie–Weiss-type behavior below 200 K, which is most likely due to short-range order in one or two dimensions. The data between 200 and 300 K were corrected for diamagnetism and fitted to a Curie–Weiss relationship χ^{-1}

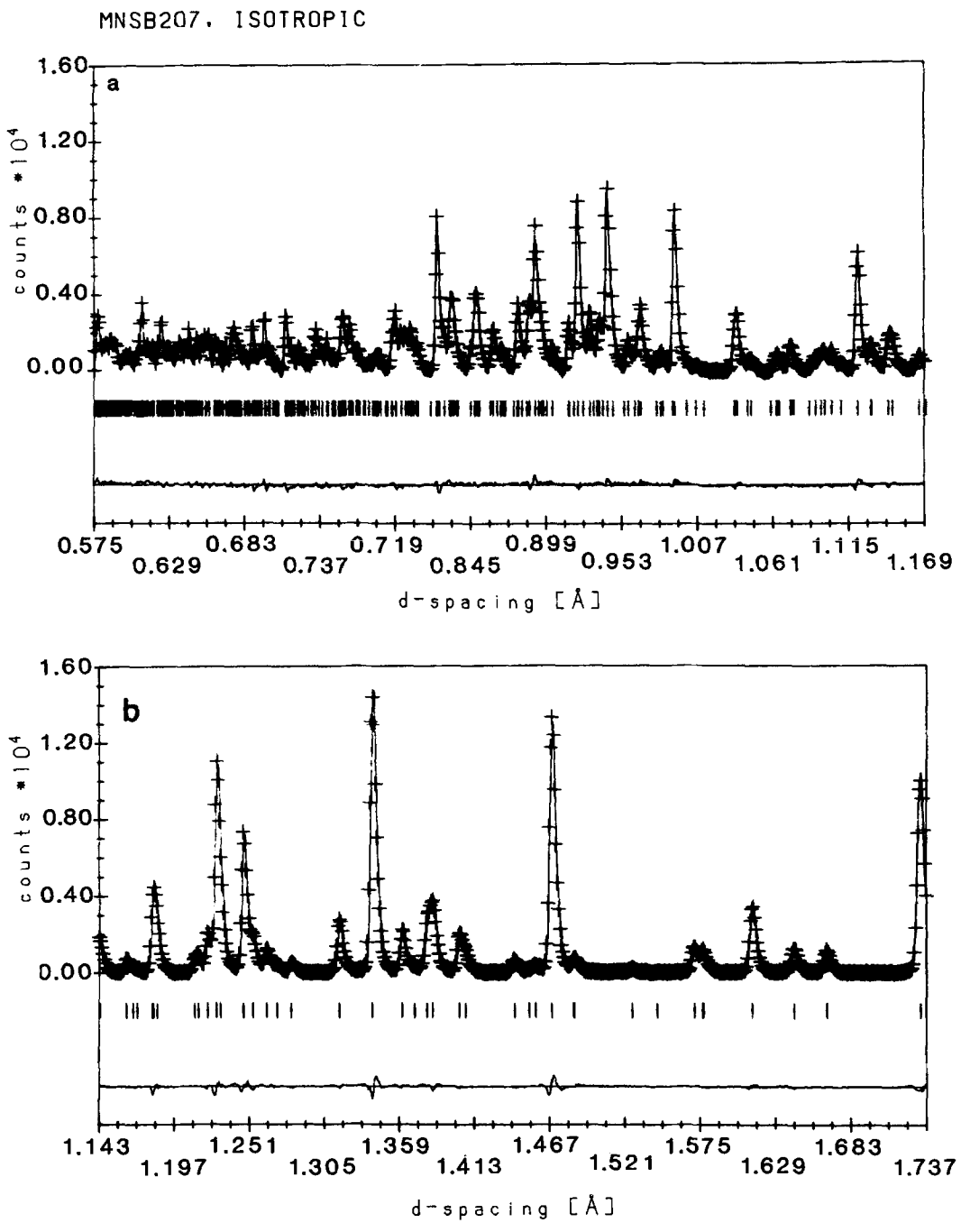

FIG. 1. The observed (+), calculated (−), and difference time-of-flight profiles for $MnSb_2O_6$ at 298 K (reflection positions are marked).

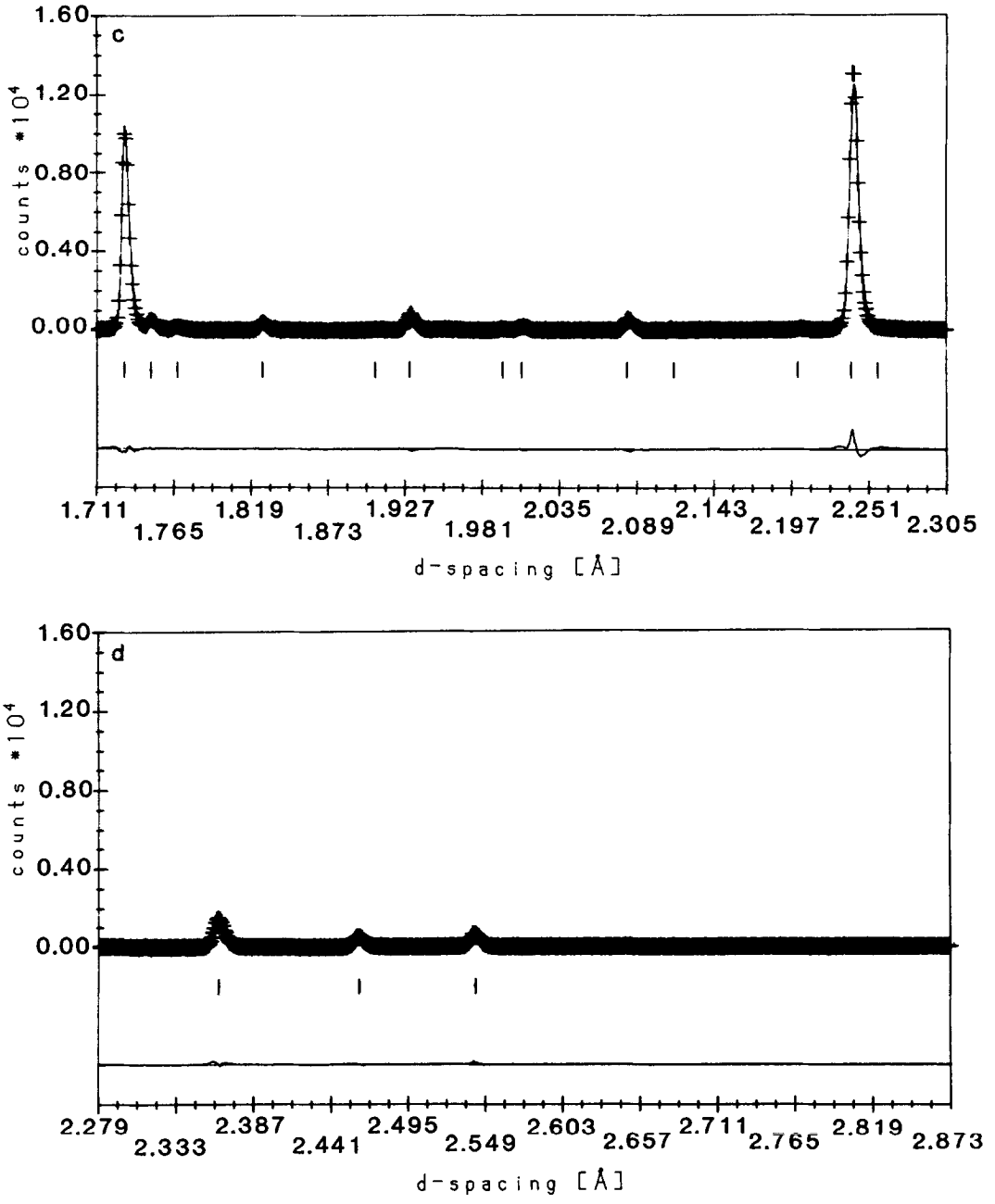

FIG. 1—*Continued.*

$= (T - \theta)/C$ giving $C = 4.15(1)$ and $\theta = -3.4(6)°$. This corresponds to a μ_{eff} of 5.76(1) μ_B which is slightly lower than the spin-only value of 5.92 μ_B.

Magnetic Structure

Below 14 K numerous magnetic reflections appear at low angles in the diffraction

TABLE I

			$MnSb_2O_6$ Trigonal $P321$, $Z = 3$		
			Scott (298 K)	IPNS (298 K)	MNR (14 K)
		a	8.8054(4)	8.8011(3)	8.802(1)
		c	4.7229(4)	4.7241(1)	4.7210(4)
		Vol.	317.13	316.905(6)	316.74(6)
Mn	(3e)	x	0.632(2)	0.6329(3)	0.6380(9)
		y	0		
		z	0		
		B (Å)	1.42(43)	0.41(3)	0.03(3)
Sb1	(1a)	x	0		
		y	0		
		z	0		
		B (Å^2)	1.45(15)	0.46(5)	0.03(3)
Sb2	(2d)	x	$\frac{1}{3}$		
		y	$\frac{2}{3}$		
		z	0.509(9)	0.5060(6)	0.507(2)
		B (Å^2)	1.45(15)	0.27(4)	0.03(3)
Sb3	(3f)	x	0.305(1)	0.3045(2)	0.3074(7)
		y	0		
		z	$\frac{1}{2}$		
		B (Å^2)	1.45(15)	0.24(3)	0.03(3)
O1	(6g)	x	0.095(11)	0.1049(2)	0.1013(7)
		y	0.885(6)	0.8930(2)	0.8905(5)
		z	0.766(8)	0.7629(2)	0.7644(7)
		B (Å^2)	1.15(63)	0.49(2)	0.03(3)
O2	(6g)	x	0.474(12)	0.4747(2)	0.4724(9)
		y	0.592(10)	0.5892(2)	0.5898(5)
		z	0.744(10)	0.7282(3)	0.730(1)
		B (Å^2)	1.15(63)	0.44(2)	0.03(3)
O3	(6g)	x	0.229(9)	0.2247(2)	0.2235(7)
		y	0.768(12)	0.7790(2)	0.7736(8)
		z	0.279(10)	0.2818(3)	0.2842(8)
		B (Å^2)	1.15(63)	0.42(2)	0.03(3)
R_{wp}[a]				5.7%	6.7%
R_p				4.0%	5.0%
R_{nuc}				5.1%	4.1%
R_{exp}				3.0%	1.7%
No. data points				4799	965
Ind. reflections				359	134
d-Space range (Å)				0.575–2.873	0.849–5.71

[a] Weighted profile $R_{wp} = 100 \times \{[\Sigma w(Y_{obs} - Y_{calc})^2]/[\Sigma w(Y_{obs})^2]\}^{1/2}$, profile $R_p = 100 \times \Sigma|Y_{obs} - Y_{calc}|/\Sigma Y_{obs}$; nuclear $R_n = 100 \times \Sigma|I_{obs} - I_{calc}|/\Sigma I_{obs}$, expected $R_{exp} = 100 \times \{(N - P)/\Sigma w(Y_{obs})^2\}^{1/2}$.

pattern. Figure 7 shows the magnetic peaks at 7.7 K; the nuclear peaks have been removed by subtracting the 30 K data. None of these peaks can be indexed on the chemical unit cell. Attempts were made to index them on a variety of obvious hexagonal super cells ($2a$, c), (a, $2c$), and ($2a$, $2c$). The orthorhombic cell (a, $\sqrt{3}a$, c) and its obvi-

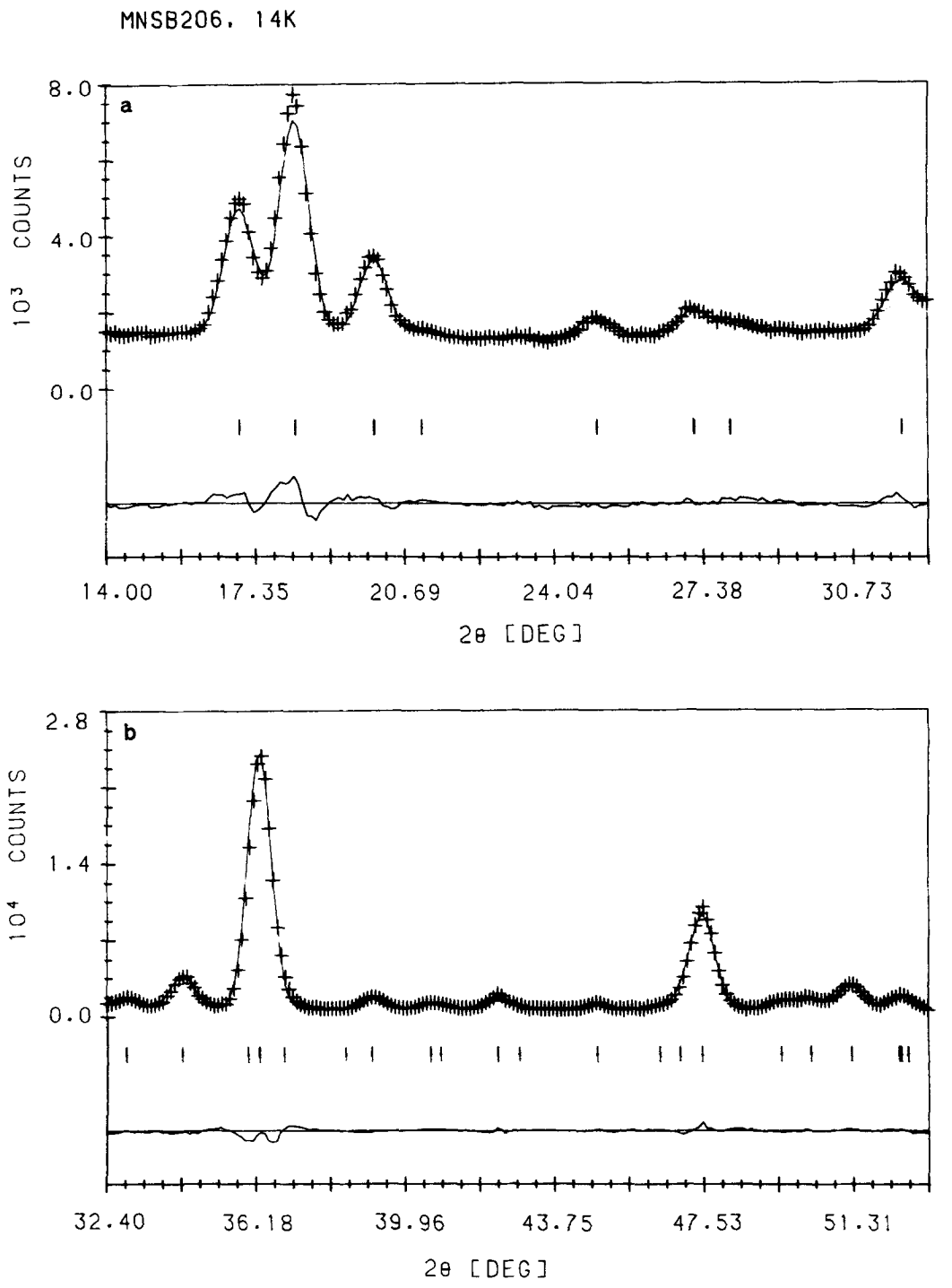

FIG. 2. The observed (+), calculated (−), and difference constant wavelength profiles for $MnSb_2O_6$ at 14 K (reflection positions are marked).

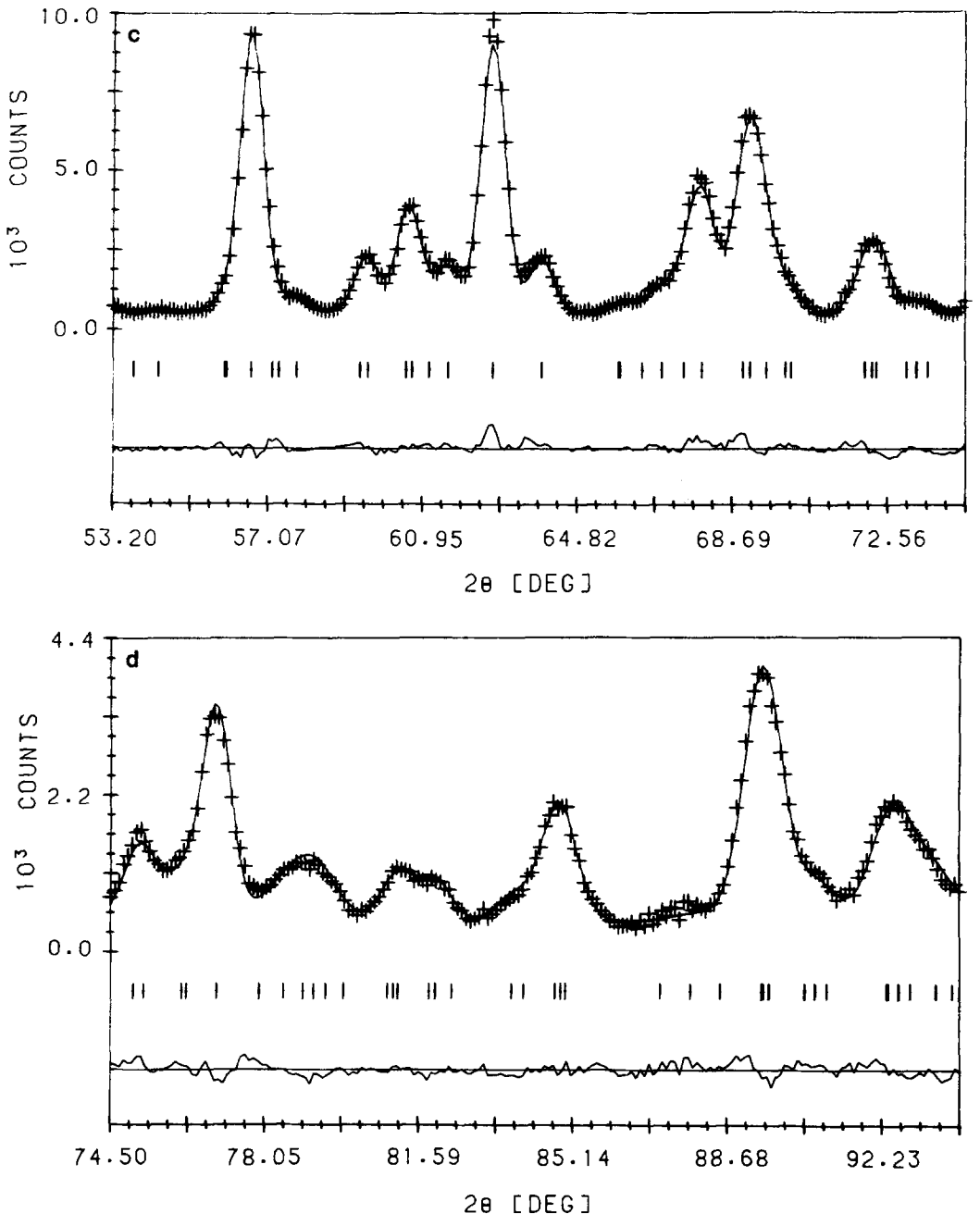

FIG. 2—*Continued.*

ous super cells were also considered, without success. The small feature at $2\theta = 19.5°$ is believed to result from subtracting two large nuclear peaks (001, 110) on either side and is probably not magnetic in origin. All magnetic peaks were fitted to Gaussians in order to obtain accurate d-spacings; the results are shown in Table III.

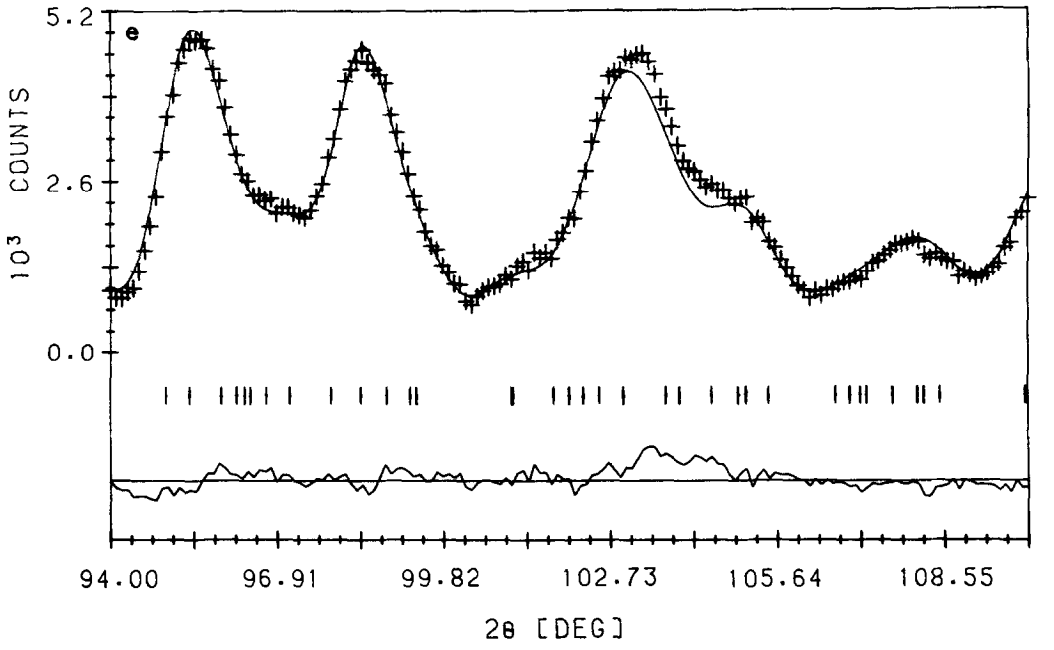

FIG. 2—*Continued.*

TABLE II

SELECTED BOND DISTANCES AND ANGLES AT 298 K IN $MnSb_2O_6$

Bond	Distance (Å)[a]		Expected [13]	Angle (°)[a]	
Mn–O	2.288(2)	Mn–O1		73.94(10)	O1–Mn–O1
	2.127(2)	Mn–O2	2.19	82.37(7)	O1–Mn–O3
	2.190(2)	Mn–O3		85.17(8)	O1–Mn–O3
				93.17(6)	O2–Mn–O3
				94.89(13)	O2–Mn–O2
				95.59(5)	O1–Mn–O2
				97.37(7)	O2–Mn–O3
Sb–O	1.966(2)	Sb1–O1		78.63(8)	O2–Sb3–O3
	1.968(2)	Sb2–O2		79.93(6)	O2–Sb2–O3
	1.989(2)	Sb2–O3	1.96	87.02(6)	O1–Sb3–O2
	1.965(2)	Sb3–O1		88.10(11)	O2–Sb3–O2
	2.018(2)	Sb3–O2		88.87(7)	O1–Sb1–O1
	1.993(2)	Sb3–O3		89.65(8)	O1–Sb1–O1
				90.14(8)	O2–Sb3–O3
				90.74(5)	O1–Sb1–O1
				92.17(5)	O2–Sb2–O3
				93.72(6)	O1–Sb3–O3
				94.18(11)	O2–Sb2–O2
				94.29(11)	O3–Sb2–O3
				96.46(8)	O1–Sb3–O3
				98.24(11)	O1–Sb3–O1

[a] Atom labels for oxygen and antimony correspond to those in Table I.

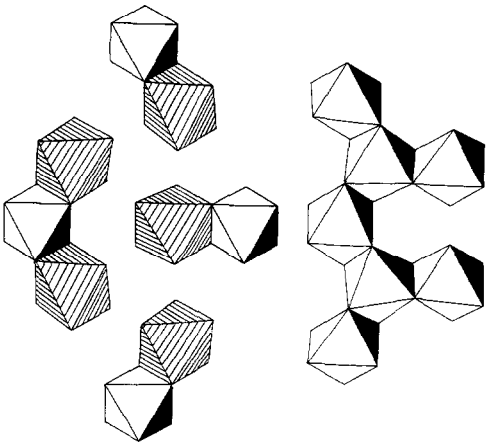

FIG. 3. One unit cell in the basal plane of $MnSb_2O_6$ showing MnO_6 (lined) and SbO_6 (shaded) edge-shared octahedra at $z = 0$ (left) and $z = \frac{1}{2}$ (right).

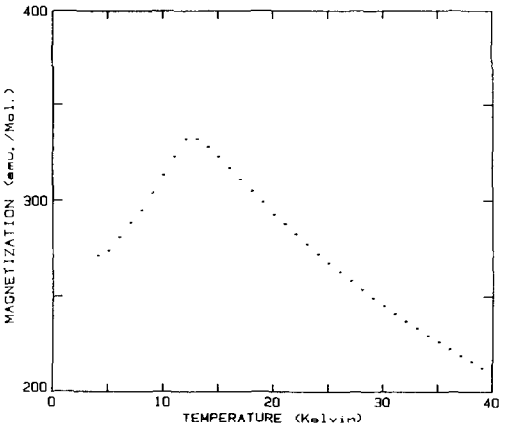

FIG. 5. Magnetization measured at 3 kOe showing onset of antiferromagnetic ordering at ≈12.5 K.

Incommensurate magnetic structures are usually described as a spiral with a propagation vector $\boldsymbol{\tau}$. Neutron scattering from such a magnetic structure occurs at satellite points in reciprocal space (*14*),

$$\mathbf{Q} = \mathbf{K} \pm \boldsymbol{\tau},$$

where $\mathbf{K}$ is a reciprocal lattice vector, $\boldsymbol{\tau}$ is the spiral propagation vector, and $\mathbf{Q}$ is the neutron scattering vector. For a single crystal, locating one satellite in reciprocal space determines τ, but determining τ from powder data is much more difficult.

In a general spiral structure the spins lie on cones about which they rotate. The spin vector on sublattice v in unit cell n can be expressed as (*15*)

$$\mathbf{S}_{nv} = \mu \sin\beta_v\{\hat{\mathbf{u}}_1 \cos(2\pi\boldsymbol{\tau} \cdot \mathbf{R}_{nv} + \phi_v) + \hat{\mathbf{u}}_2 \sin(2\pi\boldsymbol{\tau} \cdot \mathbf{R}_{nv} + \phi_v)\} + \hat{\mathbf{u}}_3\mu \cos\beta_v,$$

where μ is the magnetic moment, β_v and ϕ_v are, respectively, the cone half angle and

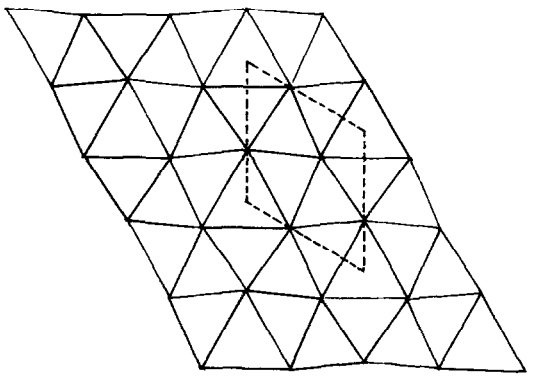

FIG. 4. Basal plane Mn^{2+} sublattice showing distorted triangular network. Unit cell is indicated by the dashed line.

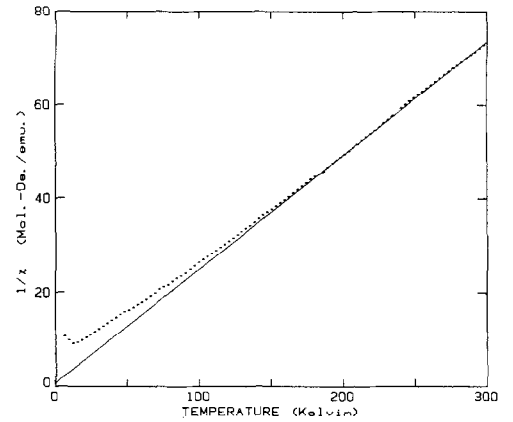

FIG. 6. Inverse susceptibility (3 kOe) data (·) and Curie–Weiss law fit (−) above 200 K for $MnSb_2O_6$.

TABLE III

POSITIONS, INTENSITIES AND FWHM'S OF $MnSb_2O_6$ MAGNETIC PEAKS

Peak	2θ (°)	d (Å)	Ref. int.	FWHM (°)
1	10.99(1)	7.27(1)	1.000(6)	0.99(1)
2	17.58(1)	4.553(4)	0.309(4)	0.78(1)
3	21.45(1)	3.739(3)	0.245(3)	0.74(1)
4	22.88(1)	3.507(3)	0.177(3)	0.76(1)
5	25.47(1)	3.157(3)	0.128(3)	0.66(1)
6	28.34(1)	2.843(2)	0.217(3)	0.74(1)
7	29.40(2)	2.742(3)	0.069(1)	0.81(3)
8	31.44(1)	2.568(2)	0.103(2)	0.81(1)

phase angle for sublattice v. The $\hat{\mathbf{u}}_i$ ($i = 1, 2$, or 3) are an arbitrary orthonormal basis with $\hat{\mathbf{u}}_3$ along the cone axis. As shown by the above expression the cone axis component of the spins does not modulate and will therefore cause some magnetic scattering to occur at normal reciprocal lattice points. No such intensity was observed in our data, thus all three β's must be $\pi/2$. As a first guess the phase angles ϕ_v were chosen to be 0, $2\pi/3$, $4\pi/3$ corresponding to a triangular spin arrangement.

With this information approximate scattering intensities can be calculated from the expression (*15*)

$$I(\mathbf{Q}) = \{Nf(\mathbf{Q})(0.27\mu)\,\Sigma_v \exp(2\pi i\mathbf{K}\cdot\mathbf{R}_v + i\phi_v)\}^2\{1 + (\mathbf{Q}\cdot\hat{\mathbf{u}}_3)^2\}/4,$$
$$\mathbf{Q} = \mathbf{K} \pm \boldsymbol{\tau},$$

where N is the number of unit cells in the scatterer and $f(\mathbf{Q})$ is the magnetic form factor. One can see that $\boldsymbol{\tau}$ only affects the satellite intensities in a minor way. For small $\mathbf{Q}$ where the form factor is appreciable the intensities are strongly dependent on the structure factor alone. Since the magnetic sublattice is pseudotriangular many of the structure factors will be close to zero, and the corresponding satellite reflections can be ignored in the determination of $\boldsymbol{\tau}$.

A computer was used to search the first zone for a vector $\boldsymbol{\tau}$ that can index the observed magnetic reflections as satellites of r.l. points with magnetic structure factors $F_{hkl} > F_{ooo}/10$. Using the variance between observed and calculated 2θ values as a measure of agreement, a list of possible τ's was generated which were then refined by a least-squares routine. A propagation vector (0.015, 0.015, 0.183) in r.l.u. gave the best

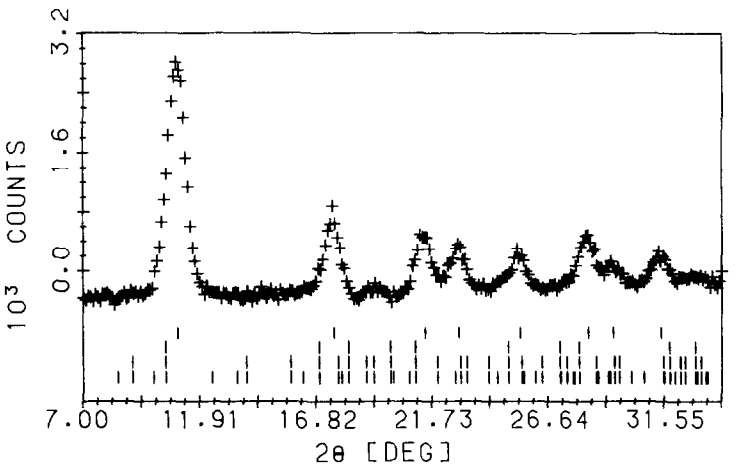

FIG. 7. Magnetic diffraction peaks for $MnSb_2O_6$ at 7.7 K. Nuclear peaks were removed by subtracting the 30 K data. Positions of the magnetic reflections (top line) along with Bragg angles for the unit cell and two super cells (orth [a, $\sqrt{3}a$, c] and hex [$2a$, $2a$, $2c$]) from top to bottom are indicated.

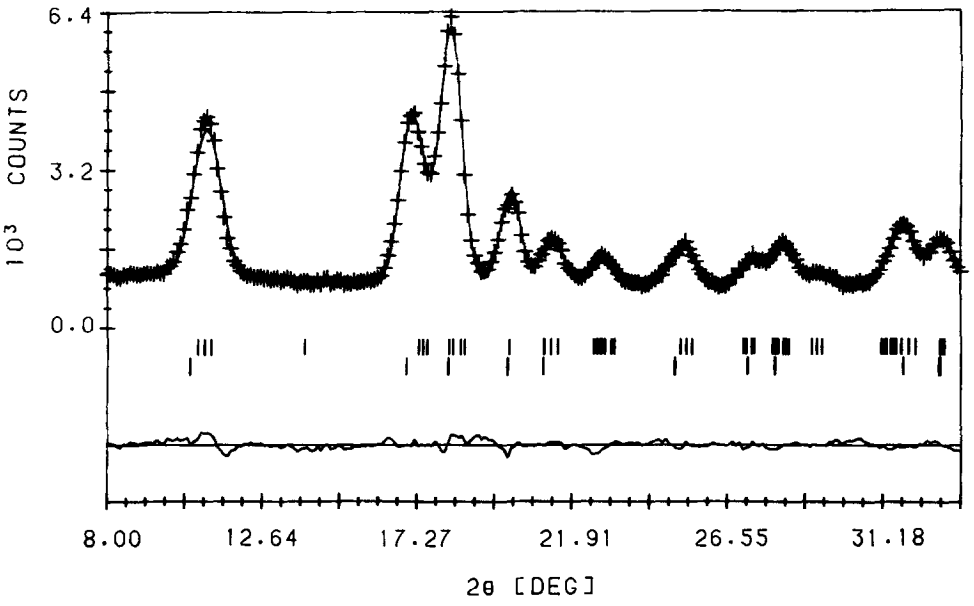

FIG. 8. Observed (+), calculated (−), and difference profiles of incommensurate magnetic structure at 7.7 K. Bragg angles of nuclear reflections (bottom line) and magnetic satellite reflections (top line) are indicated.

fit with a variance that was a factor of five less than the next best guess.

A modified curve-fitting program was used to refine the magnetic structural parameters by fitting a calculated profile to the observed powder pattern at 7.7 K. The nuclear structure, cell constants, and peak width parameters were held fixed from the 14 K refinement. Eight magnetic parameters (μ, ϕ_2, ϕ_3, τ_x, τ_y, τ_z, $u_3(\theta)$, and $u_3(\theta)$) and four profile parameters (background, background slope, overall scale, and zero angle) were refined. The cone axis u_3 was refined in polar coordinates and ϕ_1 was fixed at 0 as only the relative phases between the sublattices are important. The magnetic form factor for Mn^{2+} was taken from Watson and Freeman's calculations (*16*). Table IV shows resulting parameters for the 7.7 K data set and Fig. 8 shows the profile fit.

TABLE IV

PARAMETERS FROM PROFILE FIT OF 7.7 K DATA SET

Effective moment	μ	3.768(8) μ_B
Propagation vector	τ_x	0.013(1) r.l.u.
	τ_y	0.013(1)
	τ_z	0.179(2)
Phase angles	ϕ_2	102(3)°
	ϕ_3	239(5)°
Cone axis	u_3 (θ)	17(8)°
	u_3 (ϕ)	90(4)°

Figure 9 depicts the above spin structure with $u_3(\theta) = 0.0$ (cone axis normal to the a-direction) projected onto the basal plane. Since the cone axis is in the basal plane many of the spins have components out of the plane. The spin ordering is also modulated along the c-axis with a turn angle (about the cone axis) of about 65° between layers.

A similar analysis was carried out on the scattering data from 8 to 11.75 K with very little change in the ordered magnetic structure. An $S = \frac{5}{2}$ Brillouin function fit (Fig. 10)

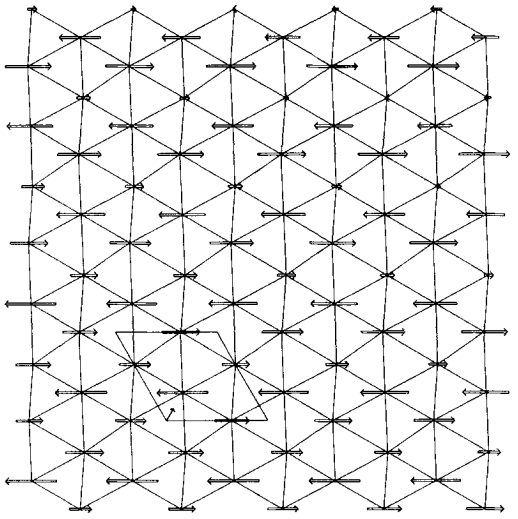

FIG. 9. Schematic illustration of a projection of the magnetic structure onto the basal plane indicating how it modulates from one unit cell to the next in the (110) direction. Spins oriented perpendicular to the page are not shown. The modulation direction is indicated by the small arrow in the unit cell.

to the magnetic moment data from 8 to 11.75 K gave an extrapolated moment of 4.6 μ_B at 0 K. The magnetic moment is smaller than the expected value for Mn^{2+}; however, other workers have also found very low Mn^{2+} moments in $RbMnBr_3$ (*17*) and $CsMnBr_3$ (*18*). The reduction in effective moment in these compounds is ascribed to quantum spin fluctuations.

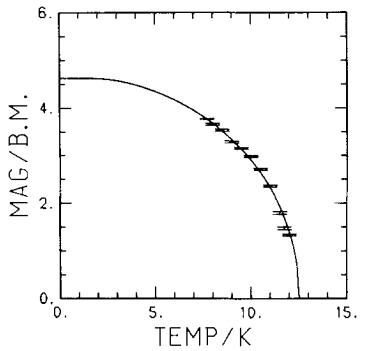

FIG. 10. Observed magnetic moments, fit to an $S = \frac{1}{2}$ Brillouin function, indicating an extrapolated zero point moment of $\approx 4.6\ \mu_B$.

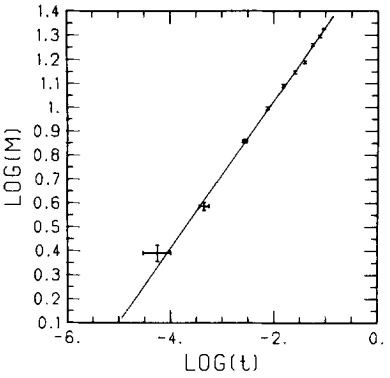

FIG. 11. Log–log plot of magnetic moment versus reduced temperature ($t = (T_c - T)/T_c$) giving $\beta = 0.31(2)$ and $T_c = 11.92(5)$ K.

Critical Region

A log–log plot (Fig. 11) of magnetic moment versus reduced temperature ($t = (T_c - T)/T_c$) with the same data set gives $\beta = 0.31(2)$ and $T_c = 11.92(5)$ K. Inspection of the 11.75 K profile refinement shows evidence of critical scattering about the magnetic peak at $2\theta = 11°$, which will cause the measured moment from the profile fit to be too large. Removing this data point does not alter β or T_c significantly, giving 0.30(2) and 11.88(5), respectively. β seems to be slightly lower than the expected Heisenberg value of 0.35 but this may be a result of the very high correlation between β and T_c when fitting the data. It is worth pointing out that if the data are fitted with T_c fixed at 12.1 K then χ^2 increases by a factor of 1.5 and β increases to 0.34(2).

Conclusions

Scott's trigonal structure for $MnSb_2O_6$ has been verified. Magnetic ordering is frustrated by the distorted triangular lattice resulting in an incommensurate magnetic structure and anomalous behavior of the

magnetic susceptibility. The critical exponent β is not inconsistent (within three standard deviations) with 3-*d* Heisenberg behavior as would be expected for Mn^{2+}.

Acknowledgments

We thank R. Hitterman and F. Rotella of IPNS for considerable assistance with all aspects of the time-of-flight neutron diffraction experiment and the complete Rietveld analysis software system. We are also grateful to Professor C. V. Stager for use of the magnetometer and Mr. G. Hewitson for considerable assistance in collecting the data. Finally, we acknowledge financial assistance from the IPNS and the Natural Science and Engineering Research Council of Canada.

References

1. S. M. Eicher, J. E. Greedan, and K. J. Lushington, *J. Solid State Chem.* **62,** 220 (1986).
2. R. Kremer and J. E. Greedan, *J. Solid State Chem.* **73,** 579 (1988).
3. K. Brandt, *Ark. Kemi Mineral. Geol.* **17a**(15), 1 (1943).
4. F. Sala and F. Trifiro, *J. Catal.* **41,** 1 (1976).
5. H. G. Scott, *J. Solid State Chem.* **66,** 171 (1987).
6. S. R. McEwen, J. Faber, Jr., and A. P. L. Turner, *Acta Metall.* **31,** 657 (1983).
7. F. Rotella, IPNS Rietveld Analysis Package, Users manual.
8. R. B. Von Dreele, J. D. Jorgensen, and C. G. Windsor, *J. Appl. Crystallogr.* **15,** 581 (1982).
9. L. Koester, *Springer Tracts Mod. Phys.* **80,** 34 (1978).
10. C. W. Tompson, D. F. R. Mildner, M. Mehregany, J. Sudol, R. Berliner, and W. B. Yelon, *J. Appl. Crystallogr.* **17,** 385 (1984).
11. H. M. Rietveld, *J. Appl. Crystallogr.* **2,** 65 (1969).
12. A. Zalkin, J. D. Forrester, and D. H. Templeton, *Acta Crystallogr.* **17,** 1408 (1964).
13. Shannon, R. D., *Acta Crystallogr. Sect. A* **32,** 751 (1976).
14. D. H. Lyons, T. A. Kaplan, K. Dwight, and N. Menyuk, *Phys. Rev.* **126,** 540 (1961).
15. J. M. Hastings and L. M. Corliss, *Phys. Rev.* **126,** 556 (1961).
16. R. E. Watson and A. J. Freeman, *Acta Crystallogr.* **14,** 27 (1961).
17. C. J. Glinka and V. J. Minkiewicz, D. E. Cox, and C. P. Khattak, "Proceedings, AIP Conference," No. 10, Part 1, p. 659 (1972).
18. M. Eibschutz, R. C. Sherwood, and F. S. L. Hsu, "Proceedings, AIP Conference," No. 17, p. 864 (1972).